PROCEEDINGS OF SCIENCE

ATLAS Results on QCD and quarkonia production

Konstantin Toms[*][†]
University of New Mexico
E-mail: `ktoms@mail.cern.ch`

First proton-proton collisions with $\sqrt{s} = 900$ GeV had place at Large Hadron Collider (LHC) at CERN and were recorded by the ATLAS detector on November 23rd of 2009. On March 30th of 2010 first collisions with $\sqrt{s} = 7$ TeV were recorded. Understanding of QCD processes in the new energy regime is essential for searches of the Higgs boson and Physics beyond the Standard Model. We present the first results on soft and hard QCD and quarkonia production by the ATLAS Experiment.

The XIXth International Workshop on High Energy Physics and Quantum Field Theory, QFTHEP2010
September 08-15, 2010
Golitsyno, Moscow, Russia

---

[*] Speaker.

[†] on behalf of the ATLAS experiment

1. Introduction

The ATLAS detector [1] is one of the two general purpose detectors of the CERN Large Hadron Collider (LHC). In this paper we present the results of physics analyses with the recorded integrated luminosity up to 40 pb^{-1} of p-p collisions with $\sqrt{s} = 900$ GeV and $\sqrt{s} = 7$ TeV center of mass energy collected in 2010–2011.

2. Soft QCD: charged particle multiplicities, Underlying Event and minimum bias

So called "soft" regime of QCD refers to the case of the small transverse momentum transfer between the initial and the final states, when the perturbative QCD calculations are not possible. The soft QCD processes include single- and double-diffractive as well as non-diffractive components contributing to inelastic scattering. For studies of such processes some phenomenological models implemented in Monte-Carlo (MC) generators are used. Parameters of such models should be tuned to data. New tune of the PYTHIA6 event generator [2] AMBT1 (ATLAS Minimum Bias Tune 1) [3] was developed for better description of the data. Term "Underlying Event" or "UE" refers to everything that happens in hadron-hadron interaction other than in the primary parton-parton interaction. UE includes beam remnants, multiple parton interactions (MPI), color recombination, all adding up to a colorless final system.

The collision data samples used in this analysis contain about 10 million of selected events with 210 million of reconstructed tracks corresponding to 190 $\mu\mathrm{b}^{-1}$ of integrated luminosity with $\sqrt{s} = 7$ TeV and about 360 thousand of selected events with 4.5 million of reconstructed tracks corresponding to 7 $\mu\mathrm{b}^{-1}$ of integrated luminosity with $\sqrt{s} = 900$ GeV. The measurements are corrected for detector effects in order to be comparable at hadron level.

The reconstructed charged particle tracks down to a transverse momentum $p_{\mathrm{T}} > 100$ MeV in the pseudorapidity region $|\eta| < 2.5$ are used.

The following distributions are measured:

$$\frac{1}{N_{ev}}\frac{dN_{ev}}{dn_{ch}}, \quad \frac{1}{N_{ev}}\frac{dN_{ch}}{d\eta}, \quad \frac{1}{N_{ev}}\frac{1}{2\pi p_{\mathrm{T}}}\frac{d^2N_{ch}}{d\eta\, dp_{\mathrm{T}}}, \quad \langle p_{\mathrm{T}}\rangle \text{ vs. } n_{ch} \tag{2.1}$$

where N_{ev} is the number of events with at least two charged particles within the kinematic range, N_{ch} is the total number of charged particles in the data sample, n_{ch} is the number of charged particles in a given event, and $\langle p_{\mathrm{T}}\rangle$ is the mean charged particle p_{T} for events with a given number of charged particles n_{ch}. Similar measurements were previously performed by ATLAS [4] [5] for events with at least one charged particle with $p_{\mathrm{T}} > 500$ MeV and $\eta < 2.5$. Also, same track selection was applied for the new minimum bias tune AMBT1; events with at least 6 charged particles were used.

The track with highest p_{T} in the event (so salled "leading" track) was used as the alignment of the energy flow from the hardest scattering process. This direction is then used to isolate regions of $\eta - \phi$ space that are sensitive to different aspects of UE. The azimuthal angular difference between charged tracks and the leading track is given by the angular magnitude $|\Delta\phi| = \phi - \phi_{\text{leading track}}$ and three distinct azimutal regions are defined as follows: $\Delta\phi < 60^\circ$ is the "towards" region, $60^\circ < \Delta\phi < 120^\circ$ is the "transverse" regions and $\Delta\phi > 120^\circ$ is the "away" region. The measured distributions for UE studies are charged particle multiplicity, charged particle scalar p_{T} sum, charged particle mean p_{T} and angular distribution. The same event, track selections (except $p_{\mathrm{T}} > 500$ MeV) and correction procedure are used for both studies.

2.1 Analysis and trigger overview

For the presented measurement the ATLAS Minimum Bias Trigger Scintillators (MBTS) were used to select the events of interest. At least one hit on either of two MBTS disks situated at $2.09 < |\eta| < 3.84$ was required. The efficiency of MBTS trigger was found to be more than 99%. Two MBTS time measurements were used to veto halo and beam-gas events. A reconstructed primary vertex was required to present in the event. The tracks used for the primary vertex reconstruction were selected within the same phase space as the tracks used for the analysis. Events with less than two tracks were discarded. In case of events with more than one vertex the events with four or more tracks associated to the second vertex were rejected.

2.1.1 Hadron and track level corrections

All distributions were corrected back to the hadron level of inelastic p-p collisions for removing detector effects. At the event level, a correction was applied to account for trigger and vertex efficiencies; a weight given by the following expression was assigned to each event as $w_{ev}(n_{sel}^{BS}) = \frac{1}{\varepsilon_{trig}(n_{sel}^{BS})} \times \frac{1}{\varepsilon_{vtx}(n_{sel}^{BS})}$ where $\varepsilon_{trig}(n_{sel}^{BS})$ and $\varepsilon_{vtx}(n_{sel}^{BS})$ are respecrively the trigger and vertex efficiencies. Both efficiencies were measured on data and parametrized as a function of selected tracks. In this procedure, the tracks are extrapolated to the nominal collision point (the beam spot) when applying the impact parameter requirements.

In addition to the event level correction, a track level correction was applied to account for tracking efficiency ($\varepsilon_{trk}(p_{\mathrm{T}},\eta)$), the rate of secondary and fake tracks ($f_{sec}(p_{\mathrm{T}},\eta)$) and the rate of tracks passing track selection that originate from the region outside the analysis kinematic range ($f_{OKR}(p_{\mathrm{T}},\eta)$). Each track is assigned a weight given by:

$$w_{trk}(n_{sel}^{BS}, p_{\mathrm{T}}, \eta) = w_{ev}(n_{sel}^{BS}) \times \frac{1}{\varepsilon_{trk}(p_{\mathrm{T}},\eta)} \times (1 - f_{sec}(p_{\mathrm{T}},\eta) - f_{OKR}(p_{\mathrm{T}},\eta)) \tag{2.2}$$

The tracking efficiency was estimated for MC events and was parametrized as a function of p_{T} and η; the main systematic uncertainty assigned to the tracking efficiency was due to the modeling of the interations of the charged particles with the material of the detector and to the estimated amount of material in the detector. The uncertainty on tracking efficiency was estimated from data by comparing to MC the bias on the reconstructed K^0 mass and the fraction of tracks in the pixel detector that are matched to a track in the full Inner Detector.

A final correction was applied to correct the selected track multiplicity n_{sel}, to the charged particle multiplicity n_{ch}. The correction implemented an iterative bayesian unfolding algorithm. According to Bayes theorem, the charged particle multiplicity probability distribution $P(n_{ch})$ is given as a function of the selected track multiplicity probability distribution $P(n_{sel})$ by:

$$P(n_{ch}) = \sum_{n_{sel}} P(n_{sel}) \times P(n_{ch}|n_{sel}), \quad P(n_{ch}|n_{sel}) = \frac{P(n_{sel}) \times P(n_{sel}|n_{ch}) \times P(n_{ch})}{P(n_{sel})} \tag{2.3}$$

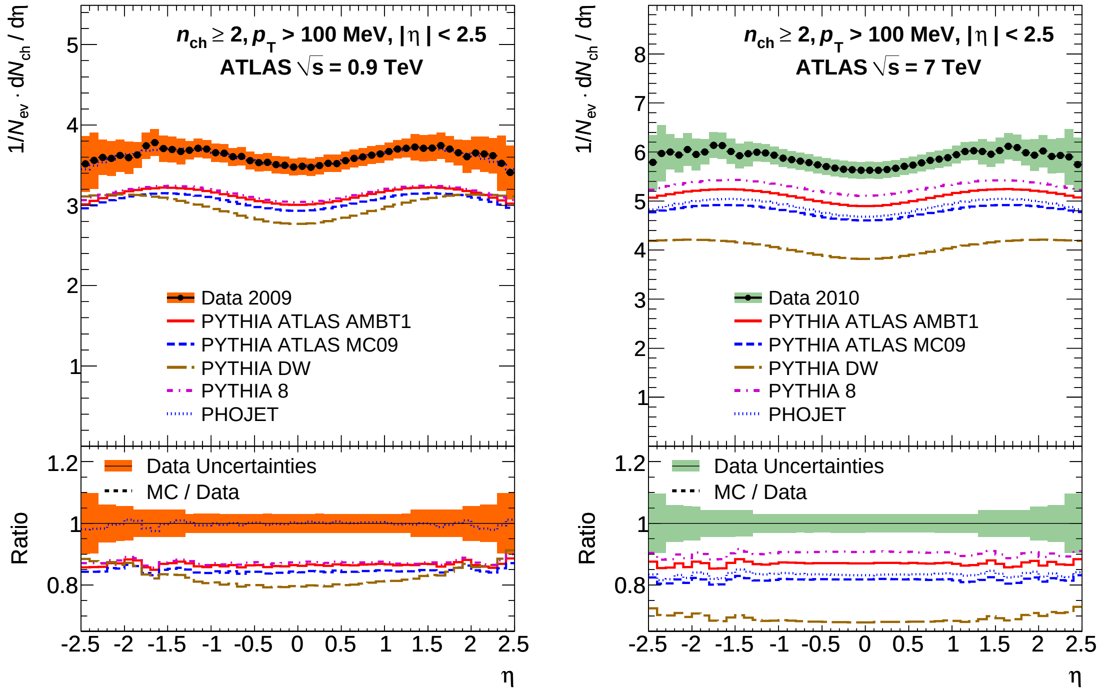

Figure 1: Charged-particle multiplicity as a function of the pseudorapidity for events with $n_{ch} \geqslant 2$, $p_T > 100$ MeV at $\sqrt{s} = 0.9$ TeV (left) and $\sqrt{s} = 7$ TeV (right). The dots represent the data and the curves the predictions from different MC models. The vertical bars represent the statistical uncertainties, while the shaded areas show statistical and systematic uncertainties added in quadrature. The bottom inserts show the ratio of the MC over the data. The values of the ratio histograms refer to the bin centroids.

where $P(n_{ch}|n_{sel})$ is the probability that an event contains n_{ch} particles when it is observed with n_{sel} tracks. This probability can be evaluated for MC events but would depend on the simulated distribution (the prior). This can be overcome by an iterative procedure where at each iteration MC events are reweighted according to the corrected distribution observed in data in the previous iteration; the procedure converges after a few iterations. Tha main systematic uncertainties that affect this unfolding procedure were found to be due to systematic uncertainty on the tracking efficiency, and to the fact that the MC events were simulated with a different p_T spectrum than the one observed from data. Both effects propagate to the migration probabilities $P(n_{ch}|n_{sel})$ which are measured for MC. A similar approach was applied to correct for non-Gaussian resolution effects in the p_T distribution.

2.2 Results

The charged particle multiplicity distributions defined in 2.1 are shown for 900 GeV and 7 TeV in Fig.1, Fig. 3 and Fig. 4 and compared to various MC predictions.

Overall no MC model gives a “perfect” description of the data. The disagreement increases for $\sqrt{s} = 7$ TeV in compare with one for $\sqrt{s} = 0.9$ TeV. The AMBT1 tune which was tuned with ATLAS data at 7 TeV shows the best agreement with the data. The ATLAS experiment measures on average

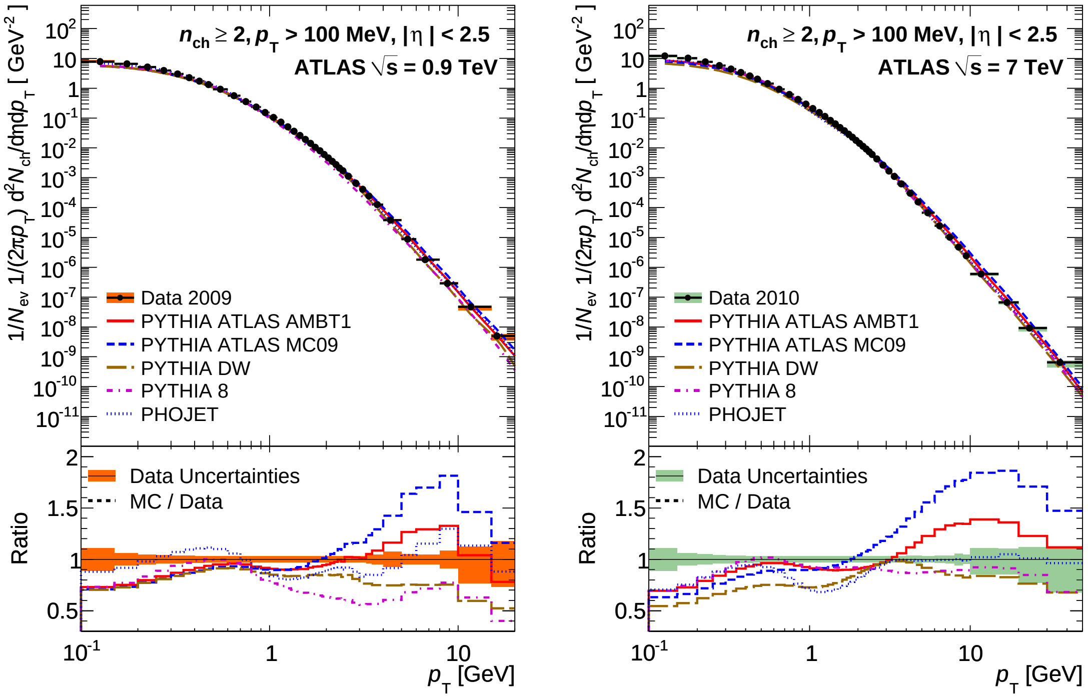

Figure 2: Charged-particle multiplicities as a function of the transverse momentum for events with $n_{ch} \geqslant 2$, $p_T > 100$ MeV at $\sqrt{s}$ = 0.9 TeV (left) and $\sqrt{s}$ = 7 TeV (right). The dots represent the data and the curves the predictions from different MC models. The vertical bars represent the statistical uncertainties, while the shaded areas show statistical and systematic uncertainties added in quadrature. The bottom inserts show the ratio of the MC over the data. The values of the ratio histograms refer to the bin centroids.

5.635±0.002(*stat*.)±0.149(*syst*.) charged particles with $p_T > 100$ MeV per unit of pseudo-rapidity at η=0 at $\sqrt{s}$ = 7 TeV, and 3.486±0.008(*stat*.)±0.077(*syst*.) at $\sqrt{s}$ = 0.9 TeV.

The measured distributions for UE are charged particle multiplicity, charged particle scalar sum P_T, charged particle mean p_T. These are shown in Fig. 5, Fig. 6, Fig. 7.

These measurements show difference between MC models and the measured distributions. All tunes underestimate the particle density by approximately 10-15% in the plateau region. There is a factor of two increase in acticity going from $\sqrt{s}$ = 0.9 TeV to $\sqrt{s}$ = 7 TeV, which is roughly consistent with the rate of increase predicted by MC models tuned to Tevatron data. In the plateau region the measured density corresponds to approximately 2.5 particles per unit η at $\sqrt{s}$ = 0.9 TeV and 5 particled at $\sqrt{s}$ = 7 TeV. The conclusion is similar for the particle densities, all the tunes underestimate the scalar sum P_T in the transverse region. There is a factor two increase of sum P_T in the plateau region going from $\sqrt{s}$ = 0.9 TeV to $\sqrt{s}$ = 7 TeV. The largest disagreement between the data and MC are observed in the transverse region.

The particle density angular correlation distributions with respect to the leading charged particle are shown in Fig. 8. The leading charged particle taken to be at $\Delta\phi$ = 0 has been excluded from the distributions. The data are shown for four different lower cut values in leading charged particle p_T. The plots are reflected around ϕ = 0. The distributions show a significant difference in shape between data and MC predictions. With the increase of the leading charged particle p_T, the

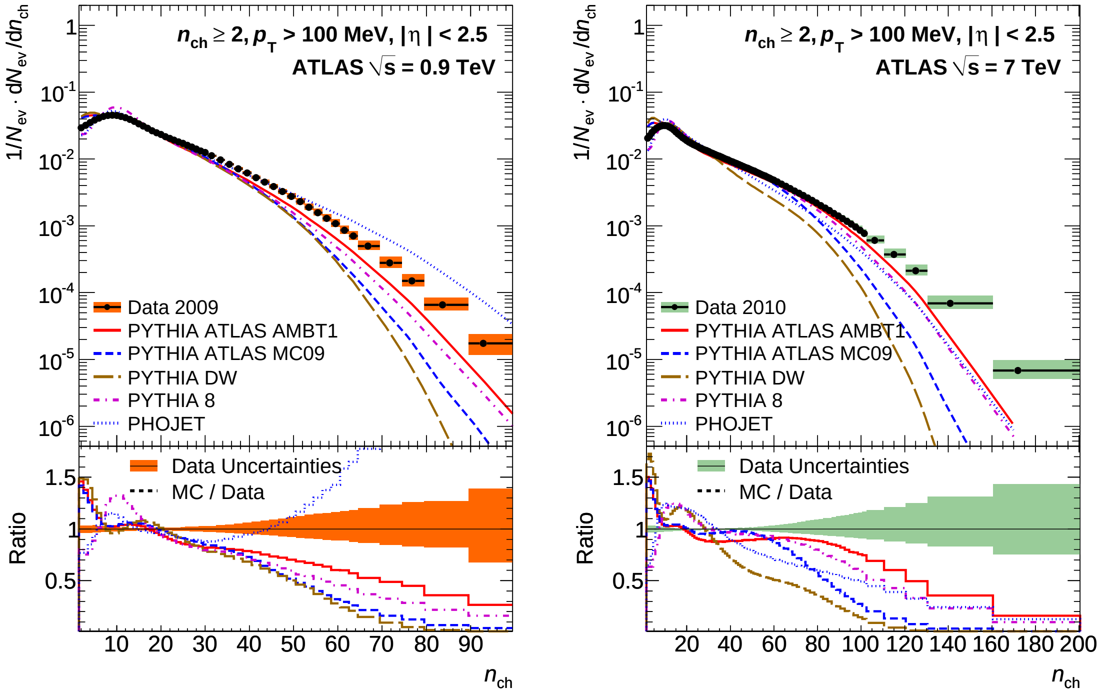

Figure 3: Charged-particle multiplicity distributions for events with $n_{ch} \geqslant 2$, $p_T > 100$ MeV at $\sqrt{s}$ = 0.9 TeV (left) and $\sqrt{s}$ = 7 TeV (right). The dots represent the data and the curves the predictions from different MC models. The vertical bars represent the statistical uncertainties, while the shaded areas show statistical and systematic uncertainties added in quadrature. The bottom inserts show the ratio of the MC over the data. The values of the ratio histograms refer to the bin centroids.

development of jet-like structure can be observed, and the corresponding sharper rise in transverse regions compared to the MC.

3. Hard QCD

The main high transverse momentum process in *p*-*p* collisions at LHC is the production of jets.

3.1 Jets: production and energy scale

First inclusive jet and dijet cross sections were measured by ATLAS detector at *sqrts* = 7 TeV with $17nb^{-1}$ of integrated luminosity. This measurement published in [6] .

Jets in ATLAS are identified using the infrared- and collinear-safe jet clustering anti-k_t algorithm [7] with resolution parameter $R = 0.4$ or $R = 0.6$. The algorithm produces geometrically well-defined (“cone-like”) jets.

Jets are formed from energy deposition four times above the noise level in the calorimeter cells, the neighbouring cells with two times above the noise level energy deposition are then iteratively added, and finally the nearest neighbours around cluster are added to accumulate the shower tail. See [8] for the details.

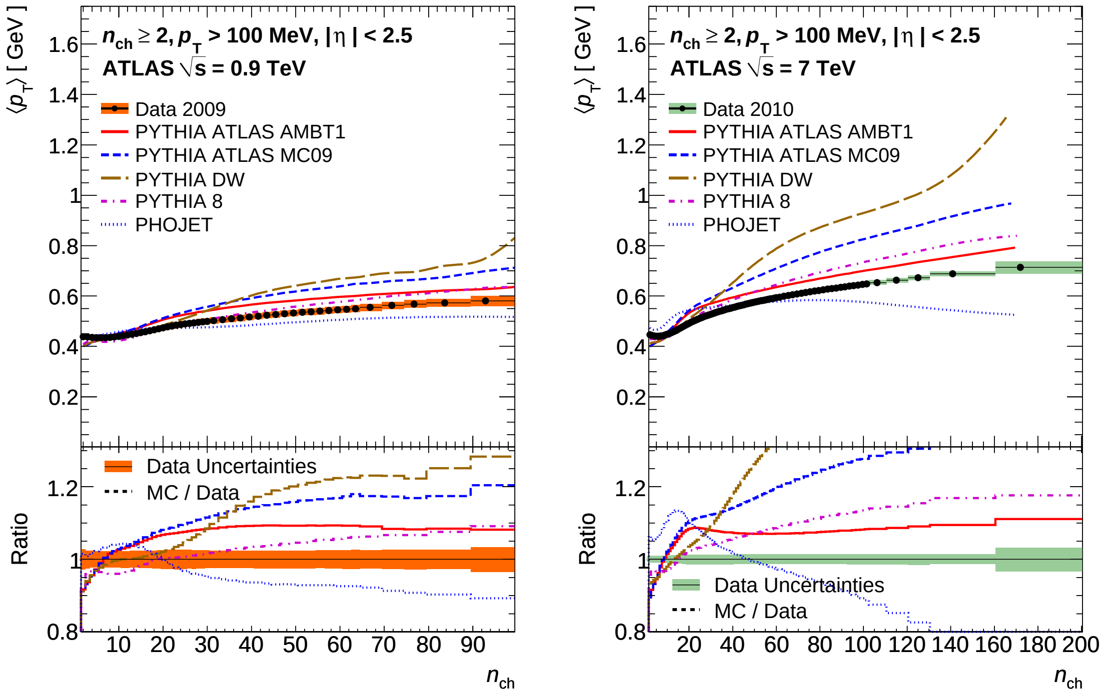

Figure 4: Average transverse momentum as a function of the number of charged particles in the event for events with $n_{ch} \geqslant 2$, $p_{\mathrm{T}} > 100$ MeV at $\sqrt{s} = 0.9$ TeV (left) and $\sqrt{s} = 7$ TeV (right). The dots represent the data and the curves the predictions from different MC models. The vertical bars represent the statistical uncertainties, while the shaded areas show statistical and systematic uncertainties added in quadrature. The bottom inserts show the ratio of the MC over the data. The values of the ratio histograms refer to the bin centroids.

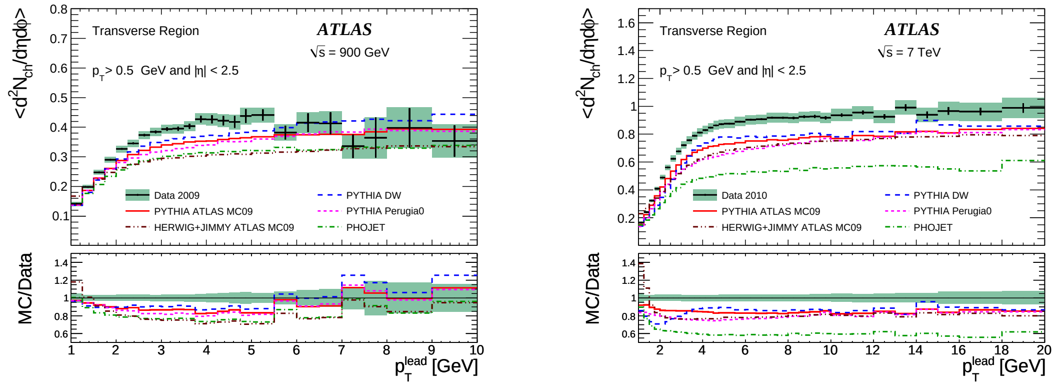

Figure 5: ATLAS data at 900 GeV (left) and at 7 TeV (right) corrected back to particle level, showing the density of the charged particles $< dN_{ch}/d\eta d\phi >$ with $p_{\mathrm{T}} > 0.5$ GeV and $|\eta| < 2.5$, as a function of p_{T}^{lead}. The data is compared with Pythia ATLAS MC09, DW and Perugia$_0$ tunes, Herwig+Jimmy ATLAS MC09 tune, and Phojet predictions. The top, middle and the bottom rows, respectively, show the transverse, toward and away regions defined by the leading charged particle. The error bars show the statistical uncertainty while the shaded area shows the combined statistical and systematic uncertainty.

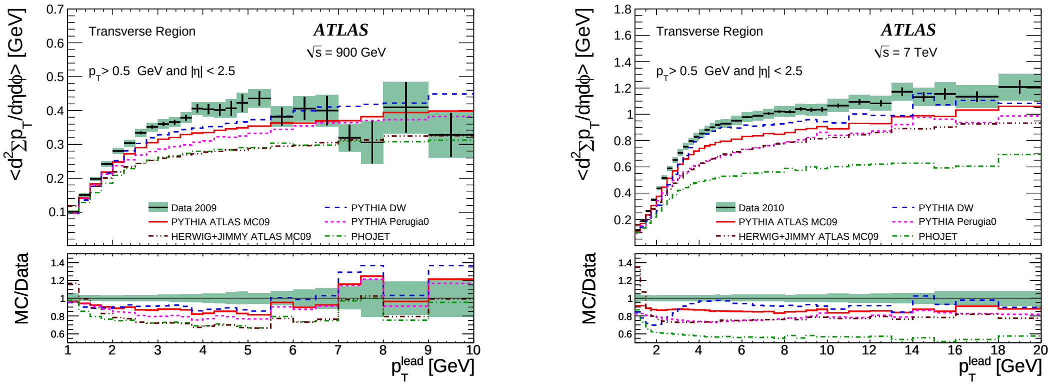

Figure 6: ATLAS data at 900 GeV (left) and at 7 TeV (right) corrected back to particle level, showing the scalar sum P_T density of the charged particles $< d^2 \sum p_T d\eta d\phi >$ with $p_T > 0.5$ GeV and $|\eta| < 2.5$, as a function of p_T^{lead}. The data is compared with Pythia ATLAS MC09, DW and Perugia$_0$ tunes, Herwig+Jimmy ATLAS MC09 tune, and Phojet predictions. The top, middle and the bottom rows, respectively, show the transverse, toward and away regions defined by the leading charged particle. The error bars show the statistical uncertainty while the shaded area shows the combined statistical and systematic uncertainty.

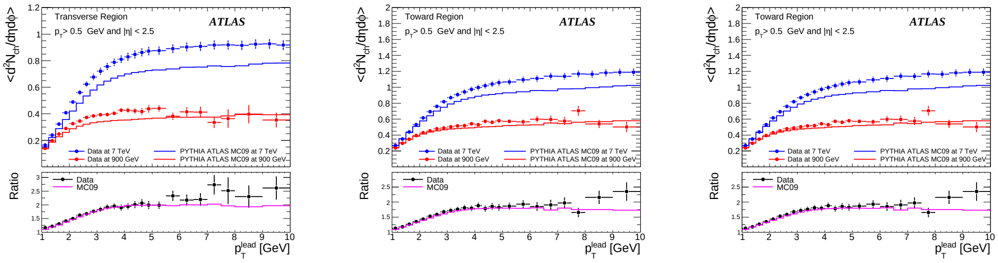

Figure 7: ATLAS data corrected back to the particle level, showing the density of charged particles $d^2N_{ch}/d\eta d\phi$ with $p_T > 0.5$ GeV and $|\eta| < 2.5$ as a function of the leading charged particle p_T, showing the comparison between data at two center-of-mass energies, with the error bars representing the combined statistical and systematic uncertainty. The bottom plots show the ratio between two center-of-mass energies for data and MC.

The jet energy scale uncertainty (JES) is found to be the dominant for that study. It was derived from test-beam data and in-situ measurements of the single hadron sesponse, central to forward di-jet balance and from systematic variations of MC simulation within the known uncertainties.

With 35 pb^{-1} of collected luminocity the overall JES uncertainty was found to be 2–4% for central jets with $p_T > 20GeV$ for $R = 0.6$, see [9] and Fig **??**.

In Fig. 9 and 10 the inclusive single-jet differential cross sections are presented as functions of jet transverse momentum and rapidity. Dijet cross sections are presented as functions of dijet mass and rapidity.The results are compared to expectations based on next-to-leading-order QCD, which agree well with the data, providing a validation of the theory in a new kinematic regime.

See [10] for more details on that study.

More ATLAS hard QCD results on dijet producton with a jet veto, b-jet and multi-jet production, dijet azimuthal decorrelations may be found in the [11], [12], [13], [14].

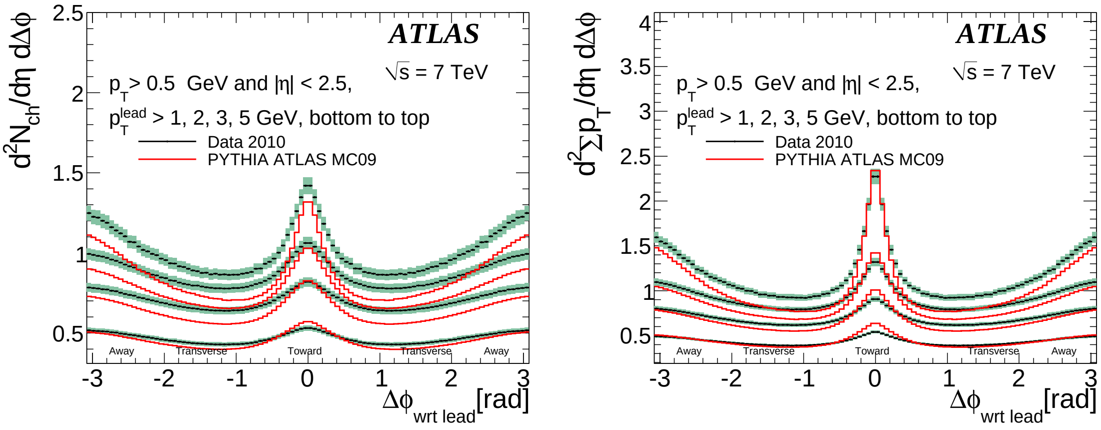

Figure 8: ATLAS data at 7 TeV corrected back to particle level, showing the ϕ distribution of charged particle densities ($d^2N_{chg}/d\eta d\Delta\phi$) (left) and p_{T} densities ($d^2p_{\mathrm{T}}/d\eta d\Delta\phi$) (right) for p_{T}> 0.5 GeV and $|\eta| <$ 2.5 with respect to the leading charged particle rotated to $\phi_{leading}$=0, excluding the leading charged particle and compared to ATLAS Pythia MC09 predictions. The distributions obtained by restricting leading charged particle p_{T}^{lead} > 1.0, 2.0, 3.0 and 5.0 GeV are overlaid. The plots were symmetrized by reflecting them about $\phi = 0$. The error bars show the statistical uncertainty while the shaded areas show the combined statistical and systematic uncertainty corresponding to each p_{T} slice.

3.2 Search for New Physics in dijet mass and angular distribution

ATLAS performed an analysis of large-p_{T} dijet using mass and angular distributions (relative to beam axis), separately or combined. Such distributions may be sensitive to various Beyond the SM models. 36 pb^{-1} of $\sqrt{s}$ = 7 TeV $p-p$ collision data have been used for this analysis. Good overall agreement with QCD was found, and ATLAS did not find any evidence for new phenomena.

Excited quarks with masses in the interval 0.60 < m_{q^*} < 2.64 TeV, axigluons with masses between 0.60 and 2.10 TeV, and Randall-Meade quantum black holes with 0.75 < M_D < 3.67 TeV (assuming 6 extra dimensions) were excluded at 95% C.L.

Quark contact interaction with a scale Λ < 9.5 TeV was excluded at 95% C.L.

See [15] for more details on that analysis.

4. Onia and J/Ψ results

4.1 *D* mesons and results on charm production

The production of the $D^{*\pm}$, $D^{\pm}$ and $D_s^{\pm}$ charm mesons have been measured with the ATLAS detector in $p-p$ collisions at $\sqrt{s}$=7 TeV using an integrated luminosity of 1.1 nb^{-1}. The charmed mesons have been reconstructed in the range of transverse momentum $p_{mathrmT}(D^*)$>3.5 GeV and pseudorapidity $|\eta(D^*)|$<2.1. The differential cross sections as a function of transverse momentum and pseudorapidity were measured for $D^{*\pm}$ and $D^{\pm}$ production. The NLO QCD predictions were found to be consistent with the data in the visible kinematic region within the large theoretical uncertainties. Using the visible D^* cross sections and an extrapolation to the full kinematic phase space, the total cross sections for D^* meson production in charm hadronisation, the strangeness-

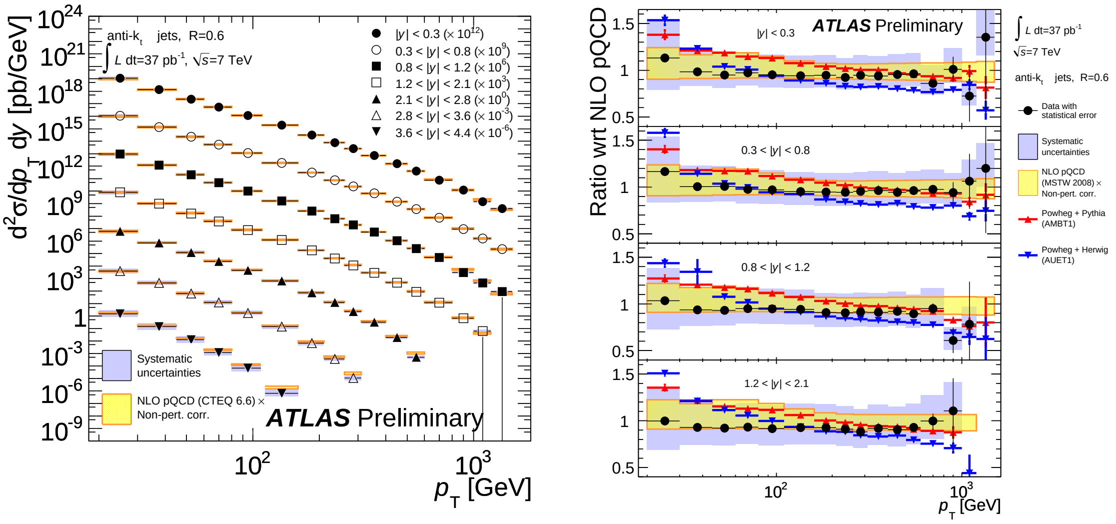

Figure 9: Left: inclusive jet double-differential cross section as a function of jet p_T in different regions of $|y|$ for jets identified using the anti-k_t algorithm with R = 0.6. For convenience, the cross sections are multiplied by the factors indicated in the legend. The data are compared to NLO pQCD calculations to which non-perturbative corrections have been applied. The error bars indicate the statistical uncertainty on the measurement, and the dark-shaded band indicates the quadratic sum of the experimental systematic uncertainties, dominated by the jet energy scale uncertainty. There is an additional overall uncertainty of 3.4% due to the luminosity measurement that is not shown. The theory uncertainty (light-shaded band) shown is the quadratic sum of uncertainties from the choice of renormalisation and factorisation scales, parton distribution functions, $\alpha_s(M_Z)$, and the modeling of non-perturbative effects. Right: The ratio of the Powheg predictions showered using either Pythia or Herwig to the NLO predictions corrected for non-perturbative effects is shown. The ratio shows only the statistical uncertainty on the Powheg prediction, and can be compared to the corresponding data ratio. The total systematic uncertainties on the theory and measurement are indicated. The NLO pQCD prediction and the Powheg ME calculations use the MSTW 2008 PDF set. Statistically insignificant data points at large pT are omitted in the ratio.

suppression factor in charm fragmentation, the fraction of D mesons produced in a vector state, and the total cross section of charm production at LHC were calculated.

In the Fig. 11 the invariant mass distributions for $D^{*\pm}$, $D^{\pm}$ and $D_s^{\pm}$ with various final states are shown.

The production of the $D^{*\pm}$, $D^{\pm}$ and $D_s^{\pm}$ charmed mesons has been measured in the kinematic region $p_T(D^*) > 3.5$ GeV and $|\eta(D^*)| < 2.1$ with the ATLAS detector in pp collisions at $\sqrt(s) = 7$ TeV. The measured visible cross sections are

$$\begin{aligned}
\sigma^{vis}(D^{*\pm}) &= 285\pm16(\text{stat.})^{+32}_{-27}(\text{syst.})\pm31(\text{lum.})\pm4(\text{br.})\ \mu\text{b},\\
\sigma^{vis}(D^{\pm}) &= 238\pm13(\text{stat.})^{+35}_{-23}(\text{syst.})\pm26(\text{lum.})\pm10(\text{br.})\ \mu\text{b},\\
\sigma^{vis}(D_s^{\pm}) &= 168\pm34(\text{stat.})^{+27}_{-25}(\text{syst.})\pm18(\text{lum.})\pm10(\text{br.})\ \mu\text{b},
\end{aligned}$$

where the last two uncertainties are due to those on the luminosity measurement and the charmed meson decay branching fractions.

The total cross section of charm production was found to be:

$$\sigma_{cc}^{tot} = 7.13\pm0.28(\text{stat.})^{+0.90}_{-0.66}(\text{syst.})\pm0.78(\text{lum.})^{+3.82}_{-1.90}(\text{extr.})\ \text{mb},$$

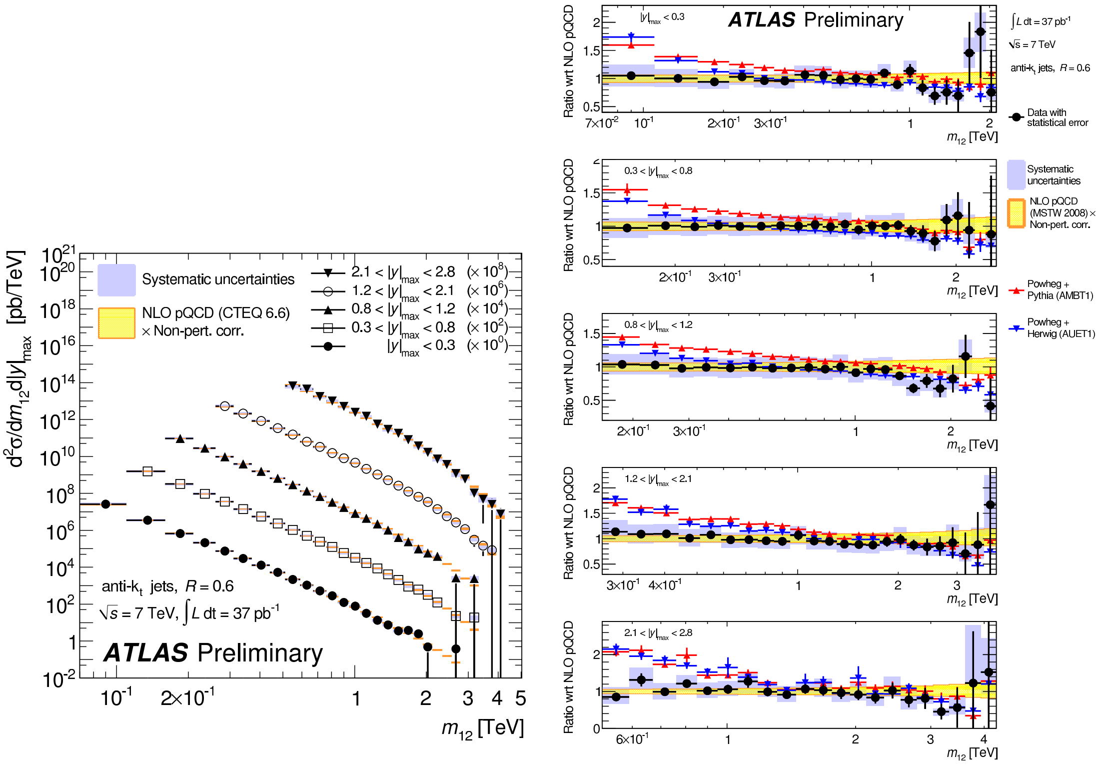

Figure 10: Left: Dijet double-differential cross section as a function of dijet mass, binned in the maximum rapidity of the two leading jets $|y|_{max}$. The results are shown for jets identified using the anti-k_t algorithm with R = 0.6. For convenience, the cross sections are multiplied by the factors indicated in the legend. The data are compared to NLO pQCD calculations to which non-perturbative corrections have been applied. The error bars indicate the statistical uncertainty on the measurement, and the dark-shaded band indicates the quadratic sum of the experimental systematic uncertainties, dominated by the jet energy scale uncertainty. There is an additional overall uncertainty of 3.4% due to the luminosity measurement that is not shown. The theory uncertainty (light-shaded band) shown is the quadratic sum of uncertainties from the parton distribution functions, $\alpha_s(M_Z)$, and the modeling of non-perturbative effects, as described in the text. The uncertainties from the renormalization and factorization scales are not included in the theory uncertainty. Right: Dijet double-differential cross section as a function of dijet mass, binned in the maximum rapidity of the two leading jets $|y|_{max}$. The results are shown for jets identified using the anti-kt algorithm with R = 0.6. The data are shown normalized to the NLO pQCD prediction using the MSTW 2008 PDF set, corrected for non-perturbative effects. The predictions from Powheg, a Monte Carlo with a NLO matrix element interfaced to a matched parton shower, hadronisation, and underlying event modeled by Pythia or Herwig, are also shown normalized to the NLO pQCD prediction. Only the statistical uncertainty is shown for the Powheg prediction.

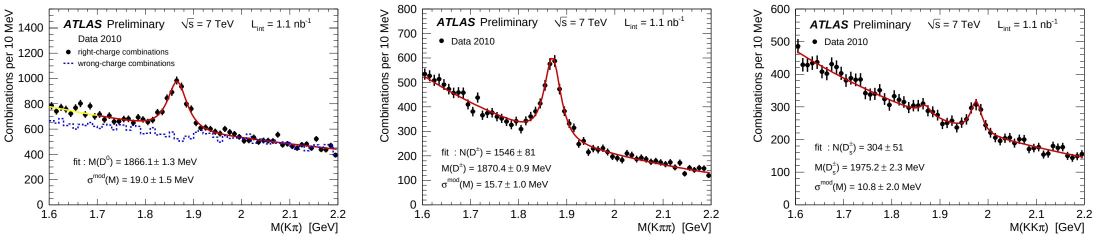

Figure 11: Left: The $M(K\pi)$ distribution for the $D^{*\pm}$ candidates (points). The dashed histogram shows the distribution for wrong-charge combinations. Center: The $M(K\pi\pi)$ distribution for the $D^{\pm}$ candidates (points). The solid curve represents a fit to the sum of a modified Gaussian function and an exponential background function. Right: The $M(KK\pi)$ distribution for the $D_s^{\pm}$ candidates (points).

where uncertainties of the fragmentation fractions were included into the extrapolation uncertainties. The uncertainties in the charmed meson decay branching fractions, which are common for the measured cross sections and fragmentation fractions, do not affect the calculation of the total cross section of charm production.

See [16] for more details on that analysis.

4.2 J/Ψ results

Well studied narrow di-muon resonances like J/Ψ, $\Psi(2S)$ and Υ family are the "standard candles" for detector performance, commissioning and for many physical analyses especially in B-physics. Di-muon spectra seen by ATLAS detector with 41 pb^{-1} of integrated luminosity of $\sqrt{s}$=7 TeV $p-p$ collisions are shown in Fig. 12 for J/Ψ and $\Psi(2S)$ (left) and Υ (right) mass regions.

The production of heavy quarkonium at hadron colliders provides particular challenges and opportunity for insight into the theory of QCD as its mechanisms of production operate at the boundary of the perturbative and non-perturbative regimes. Despite being among the most studied of the bound-quark systems, there is still no clear understanding of the mechanisms in the production of quarkonium states like the J/Ψ that can consistently explain both the production cross-section and spin-alignment measurements in e^+e^-, heavy-ion and hadron-hadron collisions (see review articles [17] and references therein).

The inclusive J/Ψ production cross section and fraction of J/Ψ mesons produced in B-hadron decays were measured as a function of the transverse momentum and rapidity of the J/Ψ, using 2.3 pb^{-1} of integrated luminosity. The cross-section is measured from a minimum p_{T} of 1 GeV to a maximum of 70 GeV and for rapidities within $|\eta| < 2.4$.

The total integrated cross-section for non-prompt J/Ψ, multiplied by the branching fraction into muons, has been measured for J/Ψ mesons produced within $|\eta| < 2.4$ and $p_{\mathrm{T}} > 7$ GeV to be:

$$
\begin{gathered}
Br(J/\Psi \to \mu^+\mu^-)\sigma(pp \to B+X \to J/\Psi X; |\eta_{J/\Psi}| < 2.4, p_{\mathrm{T}}^{J/\Psi} > 7\ \mathrm{GeV}) \\
= 23.0 \pm 0.6\ (\mathrm{stat.}) \pm 2.8\ (\mathrm{syst.}) \pm 0.2\ (\mathrm{spin}) \pm 0.8\ (\mathrm{lumi.})\ \mathrm{nb}
\end{gathered}
$$

and for J/Ψ mesons produced with $1.5 < |\eta| < 2$ and $p_{\mathrm{T}} > 1$ GeV to be:

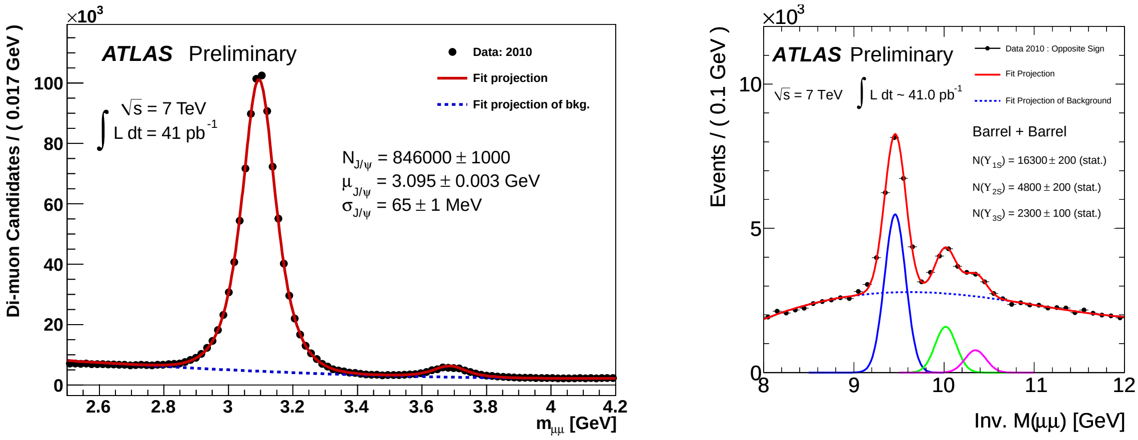

Figure 12: On the left, the $J/\Psi \to \mu^+\mu^-$ and $\Psi(2s) \to \mu^+\mu^-$ candidates are shown; plot shows all oppositely charged di-muon pairs passing vertexing with invariant masses between 2.5 and 4.2 GeV. The signal lineshape fits are both Gaussian with a third-order polynomial to model the background. On the right, the $\Upsilon(1s, 2s, 3s) \to \mu^+\mu^-$ candidates are shown; plot shows all oppositely charged di-muon pairs with invariant masses between 8 and 12 GeV, where both muons are detected in the barrel region of the ATLAS Detector. The signal lineshape fits are Gaussian with a fourth-order Chebyshev polynomial to model the background. The separations of the three peaks are fixed using the PDG masses but the absolute position on the invariant mass scale is allowed to float in the fit.

$$Br(J/\Psi \to \mu^+\mu^-)\sigma(pp \to B+X \to J/\Psi X; 1.5 < |\eta_{J/\Psi}| < 2, p_{\mathrm{T}}^{J/\Psi} > 1\,GeV)$$
$$= 61 \pm 24\ \text{(stat.)} \pm 19\ \text{(syst.)} \pm 1\ \text{(spin)} \pm 2\ \text{(lumi.) nb}$$

The total cross-section for prompt J/Ψ (times branching fraction into muons) has been measured for J/Ψ produced within $|\eta| < 2.4$ and $p_{\mathrm{T}} > 7$ GeV to be:

$$Br(J/\Psi \to \mu^+\mu^-)\sigma(pp \to \text{prompt } J/\Psi X; |\eta_{J/\Psi}| < 2.4, p_{\mathrm{T}}^{J/\Psi} > 7\ \text{GeV})$$
$$= 59 \pm 1\ \text{(stat.)} \pm 8\text{(syst.)} \pm^{9}_{6}\ \text{(spin)} \pm 2\ \text{(lumi.) nb}$$

and for J/Ψ mesons produced with $1.5 < |\eta| < 2$ and $p_{\mathrm{T}} > 1$ GeV to be:

$$Br(J/\Psi \to \mu^+\mu^-)\sigma(pp \to \text{prompt } J/\Psi X; 1.5 < |\eta_{J/\Psi}| < 2, p_{\mathrm{T}}^{J/\Psi} > 1\ \text{GeV})$$
$$= 450 \pm 70\ \text{(stat.)} \pm^{90}_{110}\ \text{(syst.)} \pm^{740}_{110}\ \text{(spin)} \pm 20\ \text{(lumi.) nb.}$$

For more details on this analysis see [18].

5. B-physics

The channel $B^{\pm} \to J/\Psi K^{\pm}$ is a reference for a variety of high-precision B-physics measurements. It may be used as a calibration tool for flavour tagging, needed for CP violation studies with B mesons (see below). The mass and lifetime measurements allow to test the performance of the ATLAS detector (e.g. alignment, magnetic field and material). Using approximately 3.4

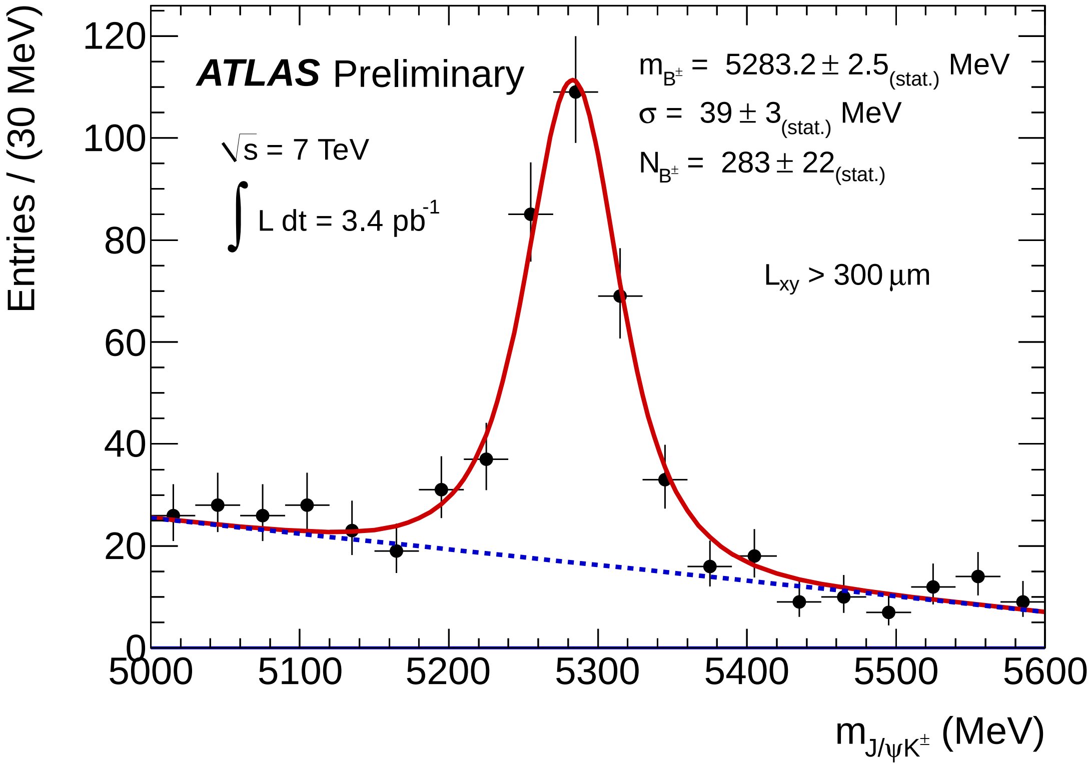

Figure 13: Invariant mass distribution of reconstructed $B^{\pm} \to J/\Psi K^{\pm}$ candidates. The points with error bars are data. The solid line is the projection of the result of the unbinned maximum likelihood fit to all $J/\Psi K^{\pm}$ candidates in the mass range 5000-5600 MeV. The dashed line is the projection for the background component of the same fit.

pb^{-1} of ATLAS $p-p$ collision data with $\sqrt{s}$ = 7 TeV the $B^{\pm}$ meson were reconstructed from the $J/\Psi K^{\pm}$ final state. The mass distributions of the signal and background were studied, the mean mass of the peak determined and the number of signal candidates extracted. Fig. 13 shows the invariant mass distribution for $B^{\pm} \to J/\Psi K^{\pm}$ candidates. The fit to the peak yields a central value of 5283.2 ± 2.5 (stat.) MeV, which is compatible with the world average of 5279.17 ± 0.29 MeV [19]. After all cuts, the total number of observed signal events is 283 ± 22 (stat.) over a background of 131 ± 13 (stat.) The details on the analysis procedure may be found in [20].

B_d^0 and B_s^0 mesons at ATLAS can be reconstructed from their exclusive decay modes $B_d^0 \to J/\Psi K^{*0}$ and $B_s^0 \to J/\Psi\phi$. The latter decay is of significant interest as it allows the measurement of the B_s^0 mixing phase, which is responsible for the CP-violation in this channel. The SM prediction for this CP violation phase is small, of the order of $\mathscr{O}(10^{-12})$, so any measured excess would be a clear indication of Beyond the SM physics. The $B_d^0 \to J/\Psi K^{*0}$ channel provides a valuable testing ground for measurements of $B_s^0 \to J/\Psi\phi$ due to its equivalent topology and similar helicity structure of the final states, with the advantage of higher statistics. The final state of the $B_d^0 \to J/\Psi K^{*0}$, with a subsequent decay of K^{*0} to charged mesons K and π allows the initial B meson flavour to be determined in a statistical way, and therefore this decay mode will be used to determine the tagging performance in CP-violation studies of other B decay channels. Early fits of B_d^0 and B_s^0

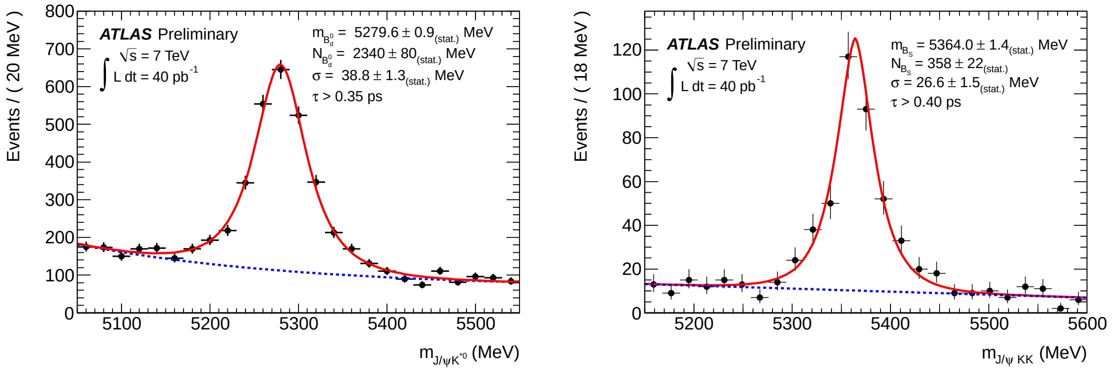

Figure 14: Invariant mass distributions of reconstructed candidates of $(B_d^0, \bar{B}_d^0) \to J/\Psi K^{0*}$ (left) and $B_s^0 \to J/\Psi\phi$ (right). The points with error bars are data. On the left, the solid line is the projection of the result of the unbinned maximum likelihood fit to all candidates in the mass range from 5050 MeV to 5550 MeV. On the right, the solid line is the projection of the result of the unbinned maximum likelihood fit to all $J/\Psi(\mu^+\mu^-)\phi(KK)$ candidates in the mass range from 5150 MeV to 5600 MeV. The dashed line is the projection for the background component of the same fit.

masses provide a good test of the performance of the ATLAS tracking system.

The B_d^0 and B_s^0 mesons produced in $sqrt(s)$=7 TeV $p-p$ collisions were observed by ATLAS with 40 pb^{-1} of integrated luminosity. The total number of observed signal events after applying all selection cuts is 2340 ± 80 (stat.) over a background of 1330 ± 60 (stat.) for B_d^0 and 358 ± 22 (stat) over a background of 90 ± 7 (stat.) for B_d^0 mesons. Fits to the reconstructed masses yield values of 5279.6 ± 0.9 stat MeV and 5364.0 ± 1.4 (stat) MeV for B_d^0 and B_s^0 respectively. Within their statistical uncertainties both numbers are consistent with the world average values 5279.5 ± 0.3 MeV (B_d^0) and 5366.3 ± 0.6 MeV (B_s^0). Fig. 14 shows the invariant mass distribution for B_d^0 (left) and B_s^0 (right) candidates passing all selection cuts. The details on the analysis procedure may be found in [21].

References

[1] G. Aad et. al. (ATLAS Collaboration), JINST **3** (2008) P07007.

[2] T. Sjostrand, S. Mrenna and P. Z. Skands, “”, JHEP **0605** (2006) 026.

[3] ATLAS Collaboration, ATLAS-CONF-2010-031 [http://cdsweb.cern.ch/record/1277665].

[4] ATLAS Collaboration, arXiv:1003.3124v1 [hep-ex].

[5] ATLAS Collaboration, ATLAS-CONF-2010-024 [http://cdsweb.cern.ch/record/1277656].

[6] ATLAS Collaboration, Eur. Phys. J. **C71** (2011) 1512.

[7] M. Cacciari, G. Salam, and G. Soyez, HEP **0804** (2008) 063.

[8] ATLAS Collaboration, JINST **3** (2008) S08003.

[9] ATLAS Collaboration, ATLAS-CONF-2011-XXX [http://cdsweb.cern.ch/record/XXXXXXX].

[10] ATLAS Collaboration, ATLAS-CONF-2011-047 [http://cdsweb.cern.ch/record/1338578].

[11] ATLAS Collaboration, ATLAS-CONF-2011-038 [http://cdsweb.cern.ch/record/1337788].

[12] ATLAS Collaboration, arXiv:1102.2696 [hep-ex].

[13] ATLAS Collaboration, ATLAS-CONF-2011-043 [http://cdsweb.cern.ch/record/1338572].

[14] ATLAS Collaboration, ATLAS-CONF-2011-056 [http://cdsweb.cern.ch/record/1342571]. ATLAS Collaboration, ATLAS-CONF-2011-057 [http://cdsweb.cern.ch/record/1343733].

[15] ATLAS Collaboration, arXiv:1103.3864v1 [hep-ex].

[16] ATLAS Collaboration, ATLAS-CONF-2011-017 [http://cdsweb.cern.ch/record/1336746].

[17] M. Kramer, Prog. Part. Nucl. Phys. **47** (2001) 141 [arXiv:hep-ph/0106120]; J. P. Lansberg, Int. J. Mod. Phys. A **21** (2006) 3857, [arXiv:hep-ph/0602091]; J. P. Lansberg et al., AIP Conf. Proc. **1038** (2008) 15, arXiv:0807.3666 [hep-ph].

[18] ATLAS Collaboration, arXiv:1104.3038v1 [hep-ex].

[19] K. Nakamura et al. J. Phys. G **37** (2010) 075021.

[20] ATLAS Collaboration, ATLAS-CONF-2010-098 [http://cdsweb.cern.ch/record/1307530].

[21] ATLAS Collaboration, ATLAS-CONF-2011-050 [http://cdsweb.cern.ch/record/1341815].